

ANALYSIS OF THE FLOW PRODUCED BY A LOW-REYNOLDS ROTOR OPTIMIZED FOR LOW NOISE APPLICATIONS. PART 1: AERODYNAMICS

Nicolas Gourdain^{*†}, Ronan Serré[†], Thierry Jardin[†], Gregory Delattre[‡] and J.-M. Moschetta[†]

[†] Dpt. of Aerodynamics, Energetics and Propulsion (DAEP), ISAE-Supaero, Toulouse, France

[‡] Dpt. of Aerodynamics Aeroelasticity Acoustics (DAAA), ONERA, Meudon, France

ABSTRACT

The demand in Micro-Air Vehicles (MAV) is increasing as well as their potential missions. Whether for discretion in military operations or noise pollution in civilian use, noise reduction of MAV is a goal to achieve. Aeroacoustic research has long been focusing on full-scale rotorcrafts. At MAV scales however, the quantification of the numerous sources of noise is not straightforward, as a consequence of the relatively low Reynolds number that ranges typically from 10^4 to 10^5 . Reducing the noise generated aerodynamically in this domain then remains an open topic. This two-parts contribution describes a numerical methodology to achieve noise reduction by optimization of MAV rotors. Three different propellers are further analyzed using high-fidelity numerical approaches, including unsteady Reynolds Averaged Navier-Stokes (URANS) simulations and Large Eddy Simulations using a Lattice Boltzmann Method (LES-LBM). That strategy will give insight on the flow features around the propellers yielding solutions to achieve noise reduction. The first part of the contribution focuses on the aerodynamic comparison between the numerical methods and the experimental measurements, in terms of loading distribution along the blade radius and global performances such as thrust and torque. A detailed study has been done also to estimate the typical turbulent scales that is generated by the tip vortex, which impacts the leading edge of the following blade. A direct computation of the far-field noise is also reported for the different blade designs.

ABBREVIATION AND SYMBOLS

C :	Blade chord	m
C_p :	Pressure coefficient	-
C_Q :	Torque coefficient	-
C_T :	Thrust coefficient	-
f :	Rotor frequency	s^{-1}
k :	Turbulent kinetic energy	$m^2 \cdot s^{-2}$
R :	Radius at the rotor tip	m
Ω :	Rotation rate	$rad \cdot s^{-1}$
V_i :	Velocity component	$m \cdot s^{-1}$
z :	streamwise direction	m
r :	spanwise direction	m
λ :	Taylor microscale	m
η :	Kolmogorov length scale	m
θ :	azimutal direction	rad

INTRODUCTION

The demand for Micro air vehicles (MAVs) is increasing, both for civil (rescue missions, archaeology investigations) and military (surveillance, recognition) applications. However, some recent studies indicate that the noise generated by small unmanned air vehicles is more disturbing for people than any other kind of vehicle [1]. In that regards,

the need to reduce the noise emitted by such MAVs is thus of paramount importance, especially in urban environment. The noise related to the propeller is shared between to the tonal noise (blade passing frequency and its harmonics) and the broadband noise, related to three sources [2]: the interaction noise (due to the impact of turbulence on the blade leading edge) [3], the trailing edge noise and the vortex shedding noise. The objective of the present work is to study the aerodynamic mechanisms that are responsible for the interaction noise.

The interaction between the rotor blades is mainly related to the interaction between the tip vortex that is generated by blade, which then impact the leading edge of the following blade. Such phenomenon is known as the Blade Vortex Interaction (BVI) and has been largely studied for forward flight [4, 5]. However, studies that report BVI in hover flight are uncommon.

From a numerical perspective, the main difficulties to accurately predict such interaction between the rotor blades are related to the relative motion between the blades (that requires to consider the whole propeller) and the accurate prediction of the turbulent flow field in the vicinity of the blade leading edge. MAVs operate at Reynolds numbers ranging from 10^4 to 10^5 where laminar to turbulent transi-

tion of boundary layers are commonly observed. A common method to simulate such flows is the unsteady Reynolds Averaged Navier-Stokes (RANS) approach, which avoids the simulation of the full turbulent spectrum by modeling the effects of all turbulence scales. With the increase in computing power, Large Eddy Simulation (LES) emerges as a promising technique to improve the reliability of flow solver predictions, with several works reported in the literature showing that LES (or detached eddy simulation) lead to significant improvements both in the understanding of flow physics [6], and performance predictions of rotors [5].

The present work reports the investigations done to analyze the BVI for a rotor in hover, designed to reduce noise for MAVs. This work considers several numerical methods: Blade Element and Momentum Theory (BEMT), unsteady RANS and LES based on a Lattice-Boltzmann method (LBM). This paper is organized in six parts. First, the different rotor geometries are presented, followed by a description of the numerical methods, including the choice for boundary conditions and numerical parameters. Then, numerical predictions are compared to experimental measurements in part 3. The numerical database are analyzed with a particular focus on the tip vortex and its effect on the rotor flow in part 4. A characterisation of the turbulent flow, through an estimation of the Taylor microscale and the Kolmogorov length scale is then reported in part 5. Finally, the performance of the far field noise is performed for three different designs and presented in part 6, before to draw some conclusions and perspective to this work.

1 PRESENTATION OF THE ROTOR CONFIGURATIONS

The test case is a 3-bladed rotor, designed to reduce acoustic emissions. The rotor has been designed using the BEMT formulation as proposed by Winarto [7]. The distributions of lift and drag are estimated from the local lift and drag coefficients on 2D sections. The estimation of sectional aerodynamic performance relies on a low-fidelity approach, which consider Euler equations along a streamline coupled with an integral boundary layer formulation [8]. Such an approach demonstrated a good accuracy for low Reynolds number flows. The main characteristics of the rotor obtained with this design technique are indicated in Table 1. The airfoil section is a Gottingen 265, which is well adapted to low Reynolds number flows (thin and cambered profil). The data presented in this paper are normalized using a standard atmosphere, with temperature $T_0=288$ K and static pressure $p_0=101,325$ Pa.

In this paper, three different design are tested, as shown in Fig. 1. The original geometry is referred as the reference. The second geometry (referred as wavy) is the reference geometry which include tubercles at the leading edge: the wavelength of the sinusoidal variation is $L/R = 0.28$, which is equivalent to one blade chord and the amplitude from peak to valley

Table 1: Characteristics of the rotor test case.

Number of blades	3
Rotation rate Ω	$518.36 \text{ rad.s}^{-1}$
Tip rotor speed	45.4 m.s^{-1}
Rotor blade chord, C	0.024 m
Rotor radius, R	0.088 m
Reynolds number, Re	0.72×10^5

is $A/R = 0.05$. The third geometry (referred as shifted) is the same as the reference geometry, except that two blades are shifted along the z -axis (streamwise direction): the second blade is shifted by $z/R = -0.057$ below its initial position and the third blade is shifted by $z/R = +0.057$ above its initial position.

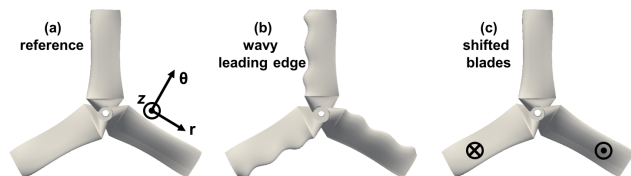


Figure 1: View of the rotor geometries.

The use of tubercles at the leading edge is a promising way to increase the aerodynamic [9] and acoustic [10, 11] performance of profiles. However, it has not been tested for rotating profiles. The shifted blade rotor should help to reduce the interaction between the tip vortex and the leading edge of the following blade.

2 NUMERICAL METHODS

Two numerical approach are used to compute the flow around the rotor: 1) an unsteady Reynolds-Averaged Navier-Stokes (RANS) approach where all turbulent scales are modelled and 2) a LES approach where the largest turbulent scales are directly simulated while the effect of the smallest ones have to be modelled.

2.1 Unsteady RANS

The three-dimensional unsteady Reynolds-Averaged Navier-Stokes (URANS) equations are solved on a cylindrical domain of diameter $20R$ and length $50R$ with the rotor located at the center. To reduce the computational cost, the flow is solved using the incompressible assumption (the maximum Mach number in this configuration does not exceed 0.15). The numerical resolution is achieved using a finite volume approach by means of StarCCM+ commercial code. The computational domain is discretized using 8×10^6 polyhedral cells with a typical size in the vicinity of the rotor of

$R/176$ (the size close to the leading edge, trailing edge and tip is decreased to $R/440$). The typical size progressively increases to reach a value of approximately $1R$ on the external boundaries of the cylindrical domain. The boundary conditions upstream and downstream the rotor are implemented as pressure conditions while the periphery of the domain is treated as a slip wall. The blades are modelled as non-slip surfaces. A full rotation is discretized with 360 time-steps. With this approach, at least 35 rotations are needed to achieve a convergence of the aerodynamic coefficient (however, 4 to 5 rotations are sufficient to estimate these coefficients with an accuracy of 2-3%). Both spatial and temporal discretizations are achieved using second order schemes. Momentum and continuity equations are solved in an uncoupled manner using a predictor-corrector approach. Specifically, a colocated variable arrangement and a Rhie-and-Chow-type pressure-velocity coupling combined with a SIMPLE-type algorithm are used [12, 13]. Finally, boundary layers are assumed fully turbulent and a $k - \epsilon$ model is employed for turbulence closure with maximum y^+ values below 1. Note that Spalart-Allmaras and $k - \omega$ models were also tested and yielded similar results to those obtained using the $k - \epsilon$ model. In addition, it was checked that the global performance are converged with respect to the typical cell size. The typical computational time needed to achieve one rotation of the rotor is 320 CPU hours (corresponding to 5h with 64 cores of a classical supercomputer).

2.2 LES-LBM

The Large-Eddy Simulation (LES) is performed by means of a Lattice-Boltzmann approach, which already demonstrated its capability to solve turbulent flows around rotor geometries [14]. Beyond its computational performance, the main advantage of LBM is that the method is stable without artificial dissipation, which makes the method equivalent to solve the Navier-Stokes equations with a high-order numerical scheme. Its drawback is that it requires the use of Cartesian grids, which dramatically increase the number of grid points close to walls. The LBM considers the discrete Boltzmann equation, a statistical equation for the kinetics of gas molecules, instead of solving directly the Navier-Stokes equations. As detailed in Refs. [15, 16], the governing equations of LBM consider the probability $f_i(x, t)$ to have a set of particles at location x and time t , with a velocity c_i :

$$f_i(x + c_i \delta t, t + \delta t) = f_i(x, t) + \Omega_{ij}(x, t) \quad (1)$$

for $[0 < i, j < N]$, where c_i is a discrete velocity of a set of N velocities and Ω_{ij} is an operator representing the internal collisions of pairs of particles. For the present 3D problems, the set of velocities is the D3Q27 scheme (27 velocities, so Eq. 1 is solved 27 times, for each velocity c_i). This kinetic scheme ensures the conservation of mass and momentum, which are related to the population of particles, f_i , as

$\rho = \sum_{i=1}^N f_i$ and $\rho \mathbf{u} = \sum_{i=1}^N f_i \mathbf{c}_i$. The collision operator is represented by a two-relaxation times model, as proposed by [17] and a regularization technique is applied to increase the stability and accuracy of the method [18, 19]. The regularization step can be seen as an explicit filtering step (that is applied at each time step), which ensures a LES formulation without subgrid scale model [20].

Three grids are designed, which all match wall-model LES (WM-LES) requirements: the dimension of the first cell in the direction normal to the wall is respectively set to $480\mu\text{m}$, $355\mu\text{m}$ and $240\mu\text{m}$ (which corresponds to $\bar{y}^+ \approx 35$, $\bar{y}^+ \approx 25$ and $\bar{y}^+ \approx 15$) for grid 0, grid 1 and grid 2. The number of grid points in the direction normal to the wall in the boundary layer ranges from 4 (grid 0) to 8 (grid 2). The airfoil is described by 100 points (grid 0), 137 points (grid 1) and 200 points (grid 2) in the chordwise direction (both pressure and suction sides) and with 183 points, 251 points and 366 points in the radial direction (from the root to the tip). To reduce the number of grid points, a hierarchical grid refinement approach is used with 7 grid levels (from one grid to the next grid, both the time step and the spatial step is divided by 2). With the finest grid, the annulus (i.e. 2π) at the tip radius is discretized with 1560 points. The computational domain is a box of size $45.R \times 45.R \times 45.R$, as shown in Fig. 2. The total number of points are respectively 23×10^6 , 153×10^6 and 179×10^6 for grid 0, grid 1 and grid 2. A full rotation of the rotor is discretized with respectively 11600, 16000 and 23200 time steps for grid 0, grid 1 and grid 2. The grid parameters for both URANS and LES are sum up in Table 2. The typical computational time needed to achieve one rotation of the rotor are 400, 1650 and 7200 CPU hours, with grid 0, grid 1 and grid 2, respectively (corresponding to 2h, 9h and 40h with 180 cores of a classical supercomputer for grid 0, grid 1 and grid 2, respectively).

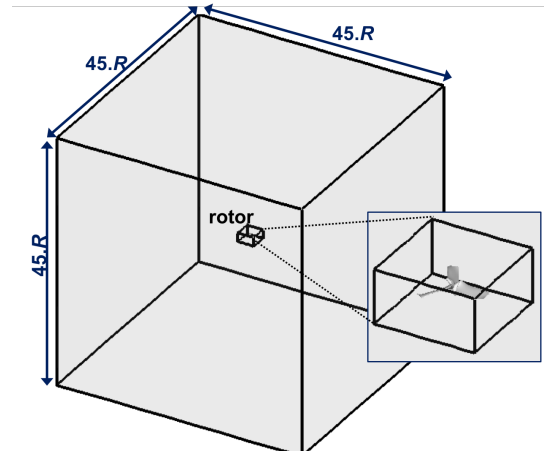


Figure 2: View of the numerical domain.

	$\frac{\Delta x}{y^+}$	$\overline{y^+}$	$\frac{\Delta z}{y^+}$	Typical cell size Δ/R
URANS	20	1	20	5.7×10^{-3}
LES-LBM, grid 0	1	35	1	5.5×10^{-3}
LES-LBM, grid 1	1	25	1	4.0×10^{-3}
LES-LBM, grid 2	1	15	1	2.7×10^{-3}

Table 2: Main grid parameters for URANS and LES (x is the chordwise direction, y is the direction normal to the wall and z is the spanwise direction).

The boundary conditions on the external faces of the computational domain are of Neumann type with zero velocity and pressure gradients. With this set of boundary conditions, the flow inside the computational box is fully driven by the rotor, so this should help to reduce the time needed to converge the torque and thrust coefficients. A sponge layer of thickness $11R$ is imposed on each face to limit spurious reflections of acoustic waves, as proposed in [21]. The movement of rotating blades are represented in the computational grid through an immersed boundary approach [22]. A wall model is considered to improve the description of the boundary layers [23]. However, due to the low number of grid points in the boundary layer, the numerical predictions close to the wall should be considered with caution.

In order to highlight the influence of mesh resolution on the rotor performance, the time evolution of the torque coefficient is plotted in Fig. 3. First, in all cases, the convergence of the torque coefficient is achieved after 3 to 4 rotor rotations, which demonstrates the good behavior of the boundary conditions. Then, the torque coefficient is underpredicted by 10% with grid 0 compared to grid 2, and by 1% with grid 1 compared to grid 2. Despite the low quality of the grid in the vicinity of the wall, the torque coefficient is no longer sensitive to the grid when considering a resolution higher or equal to grid 1. Only the data obtained on the 3 last rotations (after the 6th rotation) are considered to estimate time-averaged quantities (mean flow field, turbulent statistics). 100 samples are extracted at each rotation, so the number of samples available to compute statistics is 300. Based on the recommendations of George [24] such a set of samples allows a reasonable accuracy (below 1%) if the mean fluctuation of the considered quantity is lower than 17% of its mean value.

3 COMPARISON WITH EXPERIMENTAL DATA

The experimental rotor is manufactured using the stereolithography technology on a 3D printer with a $50\mu\text{m}$ resolution in the streamwise direction. The facility is originally designed to study noise emissions and only the global aerodynamic forces are available from a five components balance. Indeed, the comparison between experimental and numerical predictions is done only for the torque and thrust coefficients,

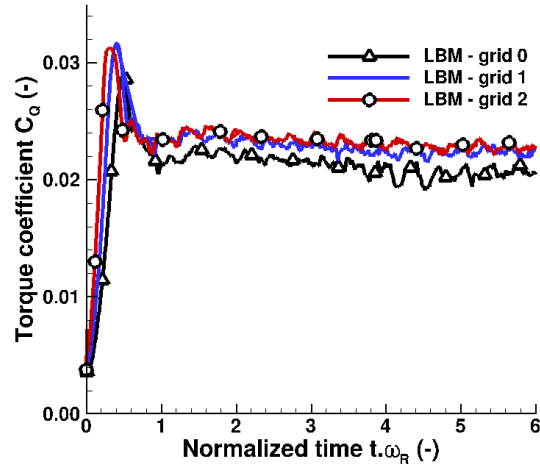


Figure 3: Torque coefficient C_Q with respect to the time: results for the three grid levels.

C_Q and C_T , defined as

$$C_T = \frac{T}{\frac{1}{2}\rho(\Omega.R)^2\pi R^2} ; C_Q = \frac{Q}{\frac{1}{2}\rho(\Omega.R)^2\pi R^3}, \quad (2)$$

with R the radius at the rotor tip. These coefficients are shown in Fig. 4. To check the general shape of the performance curve, another operating point at $\Omega = 314.16\text{rad.s}^{-1}$ (3000 rpm) has been simulated both with URANS and LES-LBM. At 3000 rpm, the accuracy of LES-LBM on thrust is very good (about 1%). Both URANS and BEMT over-predict the thrust coefficient by 15%. When considering the torque coefficient, the order of the methods regarding their accuracy is inverted: LES-LBM, URANS and BEMT over-predicts torque by 50%, 40% and 21%, respectively. At 4950 rpm, similar conclusions can be drawn: the thrust coefficient is under-predicted by 2.5% with LES-LBM, and over-predicted by 14% and 17% by URANS and BEMT, respectively. For the torque, LES-LBM, URANS and BEMT over-predicts it by 29%, 23% and 12%, respectively. It is unclear why three very different numerical methods over-predict the torque (especially the BEMT which neglect 3D effects and predicts fully attached boundary layers). Unfortunately, due to the lack of experimental data, it is not possible at the moment to identify the origin of these discrepancies.

The local thrust coefficient is plotted in Fig. 5 for the three methods. As already shown, BEMT predicts the higher thrust coefficient and LES-LBM the lowest one. From the root to $r/R = 0.4$, the three methods give the same local thrust coefficient. Then, both URANS and LES-LBM predict the same evolution until $r/R = 0.75$ while BEMT already predicts a higher value. All methods show a peak for

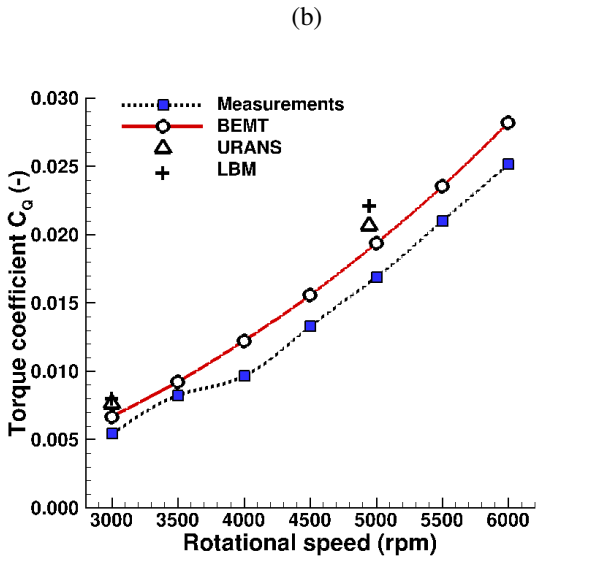
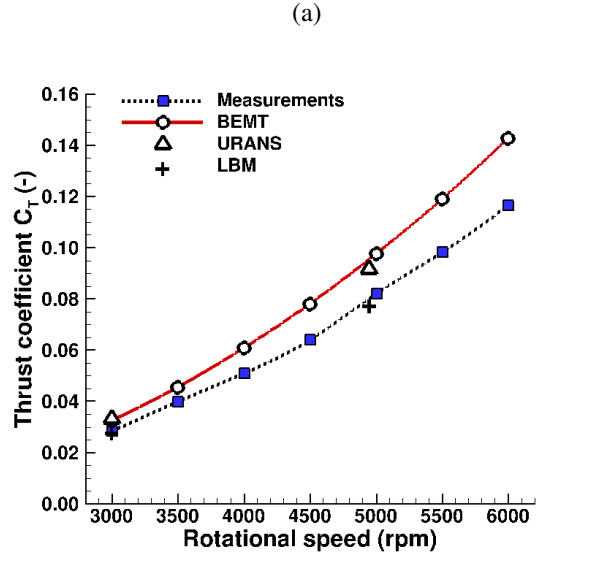


Figure 4: Comparison of global performance: (a) thrust coefficient C_T and (b) torque coefficient C_Q .

the thrust coefficient at $r/R = 0.82$ (URANS, LES-LBM) or 0.83 (BEMT). However the values of C_T at the peak are different: $C_T=0.19$ (LES-LBM), 0.22 (URANS) and 0.265 (BEMT). Beyond $r/R = 0.85$ the value of C_T decreases rapidly. Actually the main conclusion is that the three numerical methods agree reasonably well on a large part of the rotor span, but predict very different behaviour close to the tip.

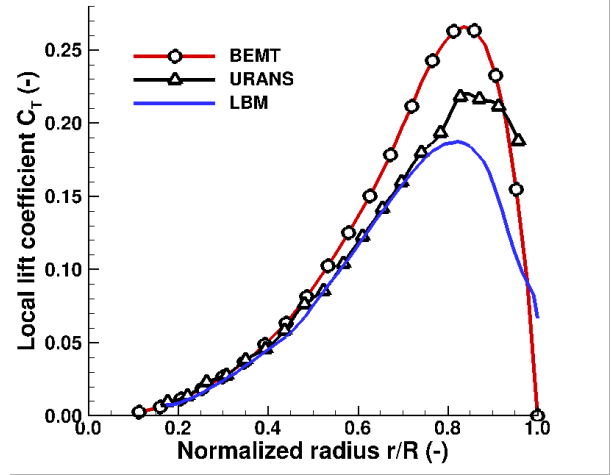


Figure 5: Local thrust coefficient.

4 ANALYSIS OF THE MEAN FLOW IN THE REFERENCE CONFIGURATION

The numerical data obtained with URANS and LES-LBM are deeper analyzed for the reference configuration, for the rotation speed $\Omega = 518.36 \text{ rad.s}^{-1}$ (4950 rpm). To normalize the streamwise coordinate (z), the reference point is taken as the leading edge at the rotor tip ($z/R = 0.0$). The flow field colored with the normalized streamwise component of the velocity $V_z/(\Omega.R)$ is shown in Fig. 6, at the altitude $z/R = 0$, that corresponds to a plane that intersects the blade close to the rotor trailing edge. The plane starts at $r/R = 0.05$ to $r/R = 1.15$. With the convention used, a negative value corresponds to a flow that is directed in the streamwise direction (i.e. in the "expected" direction). Similar flow patterns are observed on both URANS and LES-LBM flow fields, such as the contraction of the wake. Most of the thrust is achieved in the external part of the rotor, at a radius greater than $r/R > 0.5$. However, as expected, some discrepancies appear close to the tip. A boundary layer separation is observed on the suction side of the blade in the case of LES-LBM, with a limited effect of the tip vortex. On the URANS flow field, the influence of the tip vortex is well highlighted and its influence on the velocity field is observed even far downstream the blade.

The flow field, extracted 30% of the chord upstream the rotor leading edge, and colored with the normalized streamwise component of the velocity $V_z/(\Omega.R)$ is shown in Fig. 7. The most important effect of the rotor is observed between $0.45 < r/R < 0.8$. However, while LES-LBM shows only one unified region of high streamwise velocity ($|V_z/(\Omega.R)| > 0.3$), URANS shows two distinct zone, in-

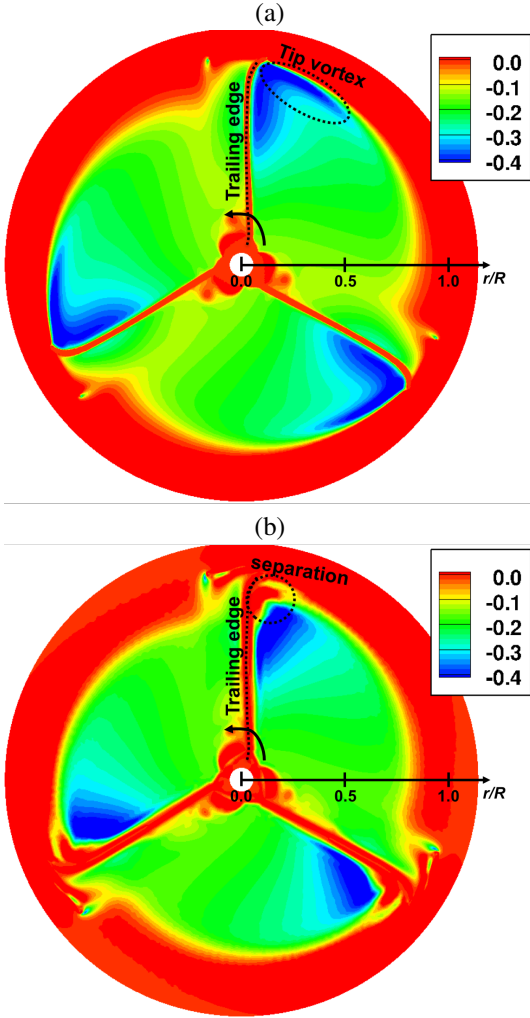


Figure 6: Time-averaged flow field colored with the normalized streamwise component of the velocity $V_z/(\omega \cdot R)$ at $z/R = 0.0$: (a) URANS and (b) LES-LBM. (Data are averaged in the reference frame of the rotor).

cluding one located at $z/R \approx -0.1$ that corresponds to the tip vortex.

To point out the influence of vortical flows in this configuration, a flow field is extracted at 50% of the chord downstream the trailing edge and colored with the normalized vorticity magnitude, as shown in Fig. 8. This view shows the wake generated downstream the blade that is then convected by the flow in the streamwise direction, with a higher speed in the vicinity of $r/R \approx 0.7$. In the case of LES-LBM a region of intense vorticity is also observed in the tip region, corresponding to the merging of the vorticity generated by the tip vortex and the boundary layer separation. The effect of the tip vortex generated by the previous blade is also visible as a

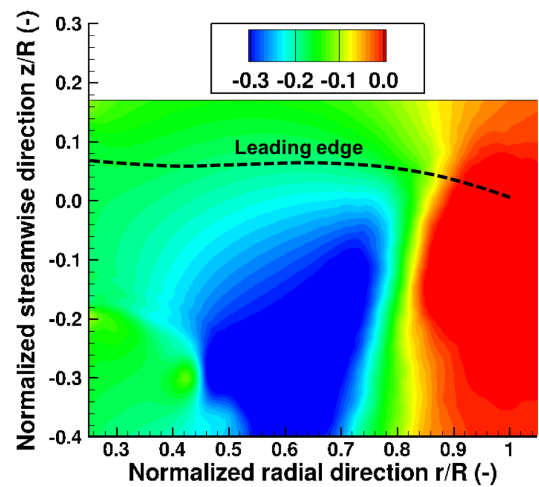
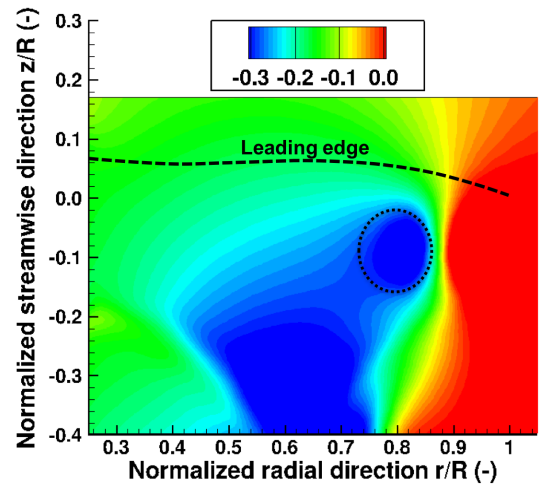


Figure 7: Time-averaged flow field colored with the normalized streamwise component of the velocity $V_z/(\omega \cdot R)$ upstream the leading edge: (a) URANS and (b) LES-LBM. The dashed line is a projection of the rotor leading edge. (Data are averaged in the reference frame of the rotor)

diffuse flow pattern (rather than as a coherent vortex), typical of a vortex breakdown phenomenon. On the contrary, in the case of URANS, only one very intense vorticity region is observed in the tip region, corresponding to a coherent vortex. The trace of the previous vortex, which is still coherent, is also visible below the rotor trailing edge. The conclusion at this step is that the performance discrepancy between LES-LBM and URANS comes from the discrepancy on the behavior of the tip vortex (breakdown in the case of LES-LBM) and the prediction of a boundary layer separation on the suction side close to the tip in the case of LES-LBM.

As reported in [25], an empirical criterion to evaluate the risk of vortex breakdown is to evaluate the Reynolds number based on the vortex characteristics Re_c and the Rossby number Ro , defined as

$$Ro = \frac{V_c}{\omega_c \cdot r_c}, \quad (3)$$

with V_c , ω_c and r_c , the axial velocity, rotation rate and radius of the vortex core, respectively. In the present case, $Re_c = 1.5 \times 10^4$ and $Ro = 0.35$. The critical value to observe vortex breakdown, is to have $Ro < 0.65$ [26]. Indeed, based on this consideration, the tip vortex observed in this configuration should breakdown. Several works reported in the literature already pointed out the difficulty to predict the vortex breakdown phenomenon with classical RANS models [27] while methods that are able to simulate, at least partially, the turbulent spectrum, such as LES or DES usually successfully reproduces it [28, 29].

Regarding the prediction of acoustic emissions, the question of potential tip vortex breakdown is of major importance: as shown in Fig. 8, in the case of vortex breakdown, the turbulence generated by the tip vortex can impact the following blade on a large part of the span, which is not the case if the vortex remains coherent.

5 ANALYSIS OF THE TURBULENT FLOW IN THE REFERENCE CONFIGURATION

The data obtained with LES-LBM are used to evaluate the turbulence properties upstream the rotor leading edge. The turbulent kinetic energy, normalized with the rotation speed $2.k/(\Omega.R)^2$, is shown in Fig. 9. Most of turbulence is produced in the region around $r/R \approx 0.8$ due to the shear layer between the rotor flow and the quiescent flow. Turbulence is also observed above the leading edge, with a turbulent intensity that represents around 5% of the rotor tip speed. This turbulence is produced mainly by the vortex breakdown, which then impact the leading edge of the following blade.

The typical turbulent scales that are seen by the rotor leading edge are evaluated by computing the Taylor microscale, that are deduced from the two-point correlations, which are defined as

$$B_{ij} = \frac{\langle V_i(r_1, t) \cdot V_j(r_2, t) \rangle}{\langle \sqrt{V_i^2(r_1, t)} \cdot \sqrt{V_j^2(r_2, t)} \rangle}. \quad (4)$$

with r_1 and r_2 two positions along the rotor span. Here, the correlation is thus considered in the spanwise direction (from the tip to the root of the rotor) using the azimuthal component of the velocity V_θ . The two-point correlation functions can be estimated for the different components of the velocity (e.g. B_{uu} , B_{vv} and B_{ww}) and static pressure. The results are presented in Fig. 10, upstream the rotor leading edge at

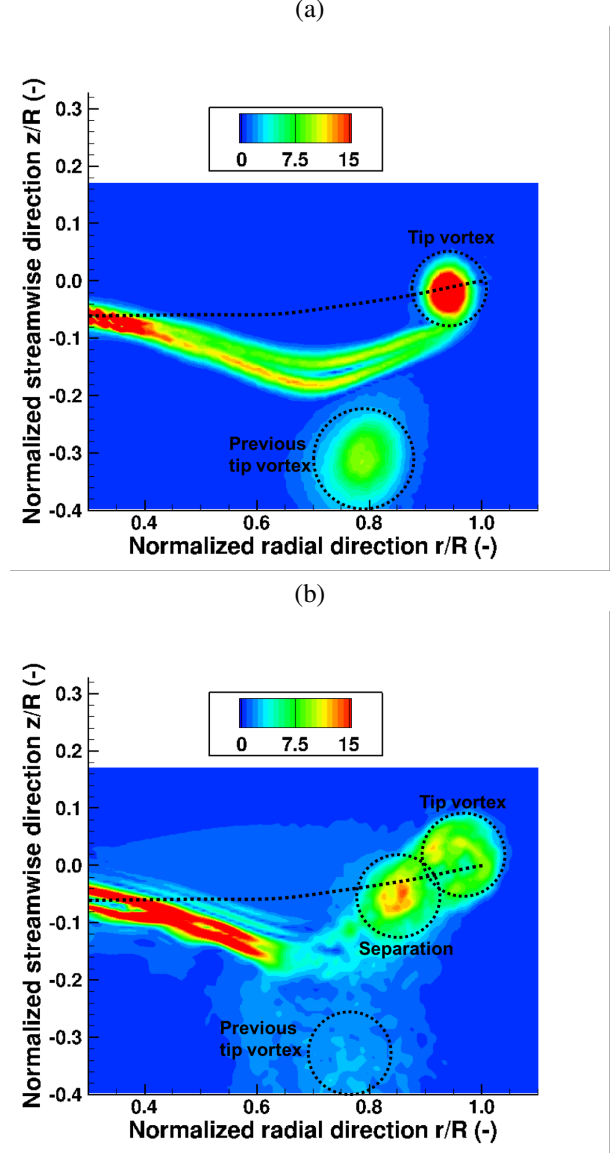


Figure 8: Time-averaged flow field colored with the vorticity magnitude ω/Ω downstream the trailing edge: (a) URANS and (b) LES-LBM. The dashed line is a projection of the rotor trailing edge. (Data are averaged in the reference frame of the rotor).

$r/R = 0.75$. The correlation function shows the same behavior for the three velocity components, V_z , V_r and V_θ but the correlation length increases by a factor 2 when considering the static pressure.

In the reference frame of the rotor, the main component of the velocity is the azimuthal component, so the spanwise correlation function is defined as $g(r) = B_{22}$. From such information it is possible to deduce the Taylor microscale λ_g ,

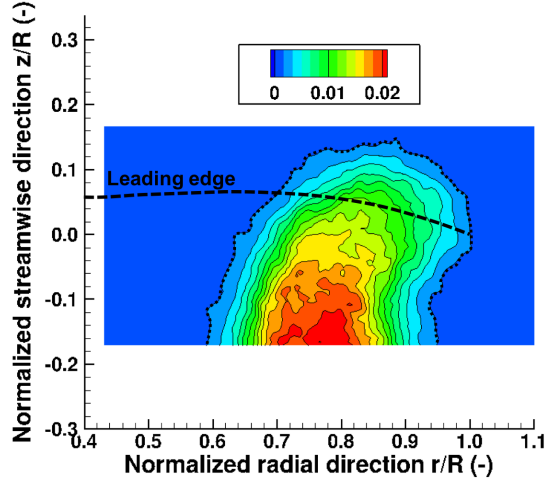


Figure 9: Time-averaged flow field colored with the normalized turbulent kinetic energy $2.k/(\Omega.R)^2$ upstream the rotor leading edge. (Data are averaged in the reference frame of the rotor).

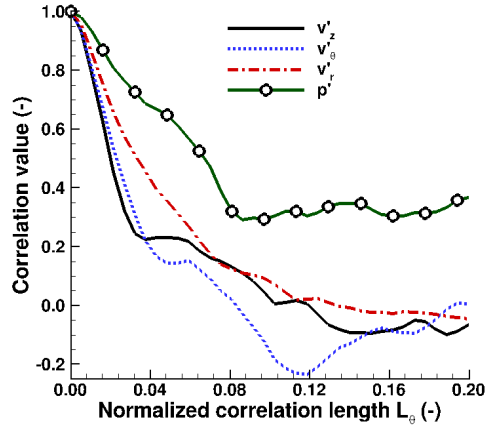


Figure 10: Normalized correlation length L_θ/R upstream the rotor leading edge at $r/R = 0.75$.

knowing the second derivative of the correlation function at $L_\theta/R=0$,

$$\lambda_g^2 = -\frac{2}{g''(0)}. \quad (5)$$

Close to the origin, it is possible to express the correlation function in a McLaurin series. By retaining only the first

order term, the correlation function writes at the origin,

$$g(L_\theta) = 1 - \frac{L_\theta^2}{\lambda_g^2}. \quad (6)$$

From Eq. 6, it is easy to provide an estimation of the Taylor microscale λ_g . Results are shown in Fig. 11 for a plane located upstream the rotor leading edge, at 30% of the rotor chord. Only the information inside the dotted line which represents a threshold for the normalized turbulent kinetic energy of $0.01 \times \Omega.R$. Below this threshold, it is assumed that the value obtained for the turbulent length scales is meaningless. The typical value for λ_g evolves from $0.02R$ (internal part of the shear layer) to $0.03R$ (external part of the shear layer, close to the tip). Two comments can be done regarding this value: 1) a very fine grid is required to properly estimate the Taylor microscale (the typical grid dimension should be one order of magnitude lower than this length scale, so the present grid is at the limit of this requirement with $\Delta = 0.002R$); 2) the value of λ_g is roughly constant all over the rotor span, which is an interesting point since it means that a control solution (or an optimized design) will have to deal with only one typical length scale.

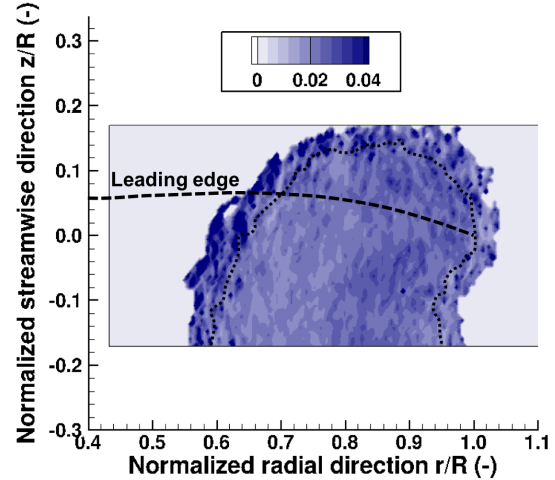


Figure 11: Normalized Taylor microscale λ_g/R , upstream the rotor leading edge. (Data are averaged in the reference frame of the rotor).

Knowing the Taylor microscale, it is possible also to estimate the Kolmogorov length scale. Assuming isotropic turbulence (which is a reasonable hypothesis upstream the rotor leading edge), the dissipation ϵ is computed with

$$\epsilon = 15\nu \frac{\overline{V_\theta^2}}{\lambda_g^2}. \quad (7)$$

Then the Kolmogorov length scale is deduced from

$$\eta_k = (\nu^3/\epsilon)^{\frac{1}{4}}. \quad (8)$$

The Kolmogorov length scale is shown in Fig. 12, upstream the rotor leading edge at 30% of the rotor chord. The typical size of the Kolmogorov length scale in the vicinity of the leading edge is around $\lambda_K/R = 0.0005$. Once again, two comments can be drawn from this analysis. 1) To achieve a grid resolution close to the Kolmogorov length scale (for this configuration), it will require to decrease the typical grid dimension Δ by a factor 4 (compared to grid 2), which in turns will increase the grid size by 4^3 (leading to a grid of about 11.5×10^9 cells). Such a direct numerical simulation is still very costly in terms of computational ressource, but it does not appear far beyond current computational capabilities. 2) If one considers the rotor radius as the largest turbulent scale, the ratio between the largest and the smallest turbulent scales is about 2000 (and the ratio between the Taylor microscale and the Kolmogorov length scale is 40). It means that at this location more than 95% of the turbulent scales can be computed with the current grid.

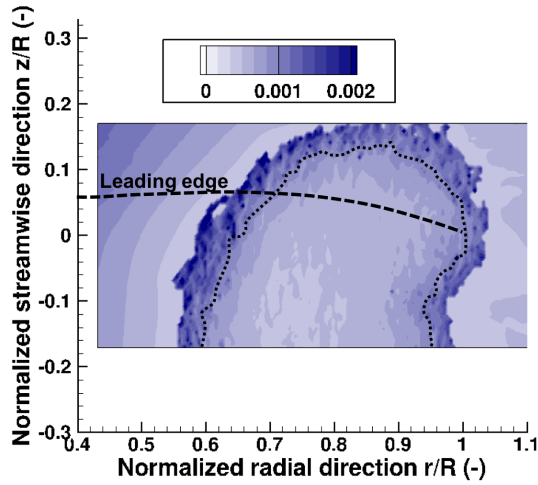


Figure 12: Normalized Kolmogorov length scale η_K/R , deduced from the dissipation ϵ , upstream the rotor leading edge. (Data are averaged in the reference frame of the rotor).

6 COMPARISON BETWEEN THREE DESIGNS

Based on the previous analysis, it is proposed to bench three different designs as presented in the first section: the reference rotor, a rotor with a wavy leading edge and a rotor with shifted blades. The simulation for each of the two last geometries is restarted from the simulation of the reference geometry to reduce the transient duration. Then 300 samples

are extracted during the three last rotations. Compared to the reference geometry, the thrust coefficient C_T is increased by 6% (wavy leading edge) and 1% (shifted blade). The torque coefficient C_Q is reduced by 4% (wavy leading edge) and increased by 1% (shifted blade).

A qualitative comparison of the flow field between the three designs can be performed in Fig. 13 that shows an instantaneous iso-surface of Q criterion, colored by the pressure coefficient $-C_p$,

$$-C_p = \frac{(p - p_0)}{(\frac{1}{2}\rho(\Omega.R)^2)}. \quad (9)$$

The flow fields of the three designs point out that three different vortices are generated close to the rotor tip (instead of only one as observed in the URANS flow field): one starts at the leading edge, one comes from the pressure side and one begins at mid-chord. The breakdown of these three vortices starts close to the trailing edge, due to the recompression. These vortices merge also with the vortex due to the separation of the suction side boundary layer, close to the tip. The mixing process between the different vortices produces turbulence that impacts the following blade (located on the left part of the picture in Fig. 13). The only exception is on Fig. 13(c) (shifted blade design) where turbulent flow patterns are driven under the leading edge of the following blade. In the case of the wavy leading edge, a vortex develops in the valley which reduces the extension of the boundary layer separation on the suction side.

A time-averaged flow field, obtained in the reference frame of the rotor, and colored with the normalized fluctuations of pressure $p'/(\frac{1}{2}\rho(\Omega.R)^2)$ is shown in Fig. 14. For the three designs, most of the pressure fluctuations are observed at two locations close to the trailing edge in the vicinity of the rotor tip (tip vortex and suction side separation). The noticeable differences between the three geometries are: 1) for the reference and the wavy leading edge cases, the three blades exhibit the same field of pressure fluctuations, but it is not the case for the shifted blade case (as expected); 2) the source of fluctuations at the rotor tip is reduced with the wavy leading edge; 3) the level of pressure fluctuations in the shifted blade geometry is reduced for two blades (the top-shifted and the middle blade) and is increased for the last one (the bottom-shifted), which shows now three sources of p' instead of two.

A time-averaged signal of normalized pressure fluctuations is shown in Fig. 15. For the reference geometry, the trailing edge is the dominant source of fluctuations, followed by the leading edge. Compared to the reference geometry, the wavy leading edge reduces the source at the trailing edge, due to its beneficial influence on the boundary layer separation, but it has no influence on the leading edge source.

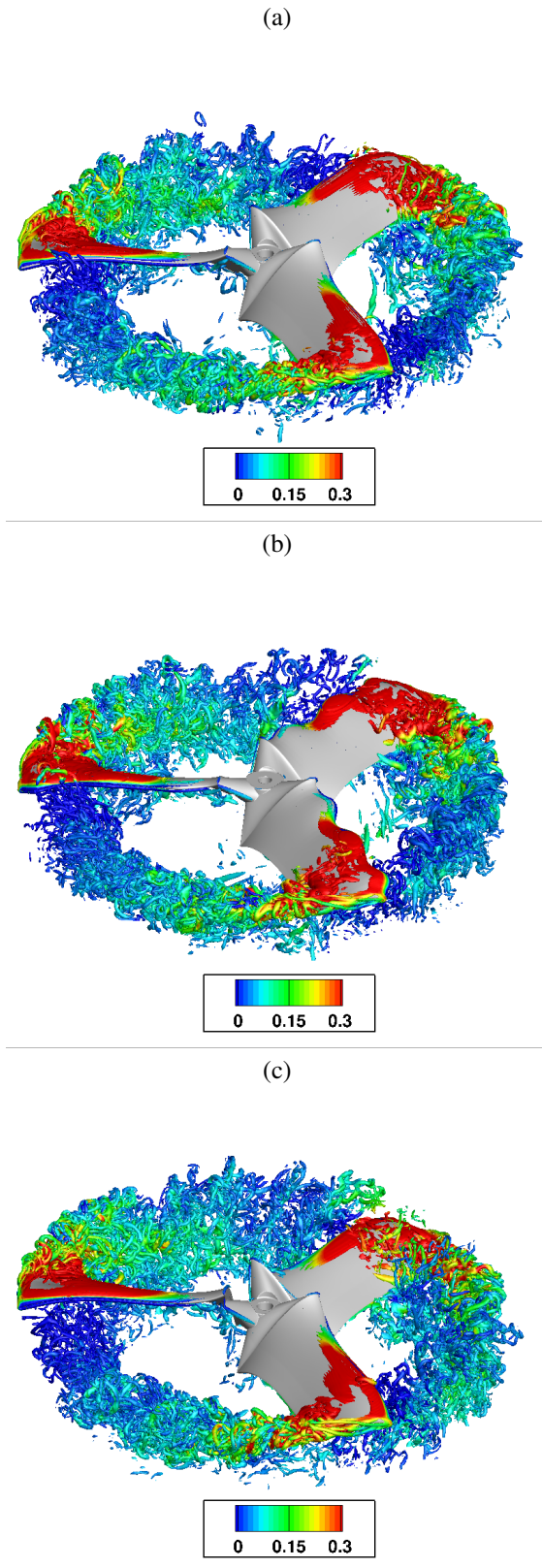


Figure 13: Instantaneous iso-surface of Q -criterion colored by the pressure coefficient $-C_p$: (a) reference geometry, (b) wavy leading edge and (c) shifted blades.

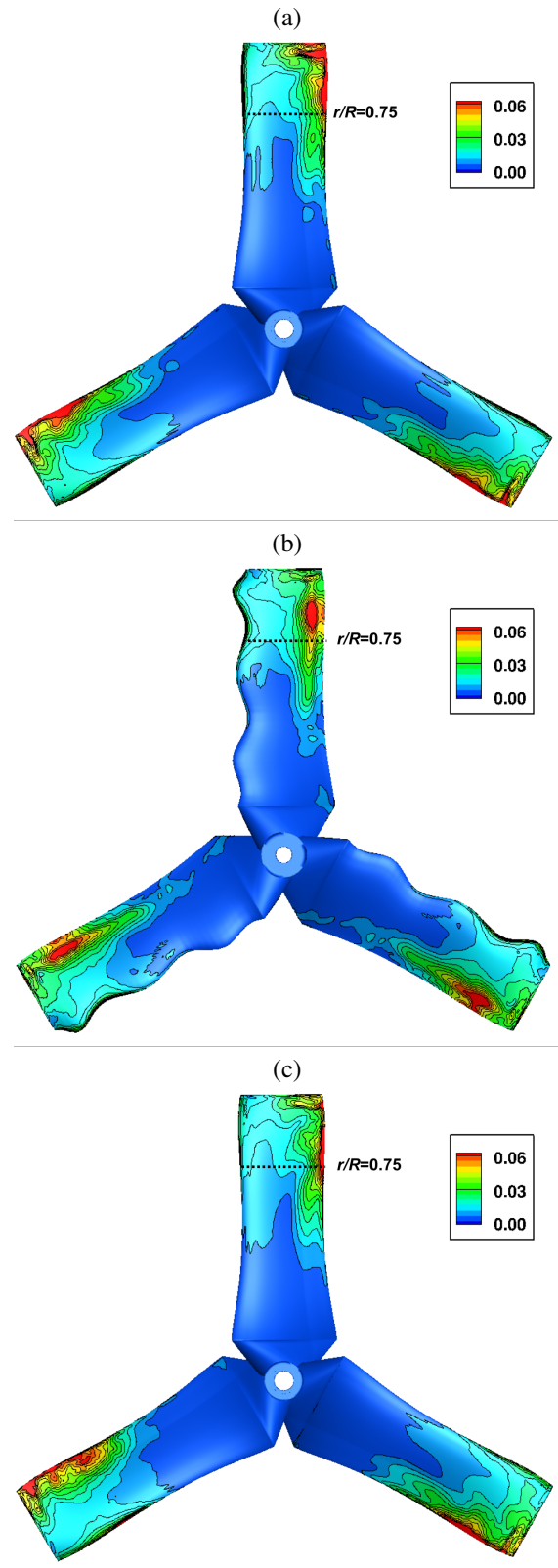


Figure 14: Time-averaged solution on the suction side colored by the normalized pressure fluctuations $p' / (\frac{1}{2} \rho (\Omega \cdot R)^2)$: (a) reference geometry, (b) wavy leading edge and (c) shifted blades.

Compared to the reference geometry, the shifted blade reduces the source at the leading edge but it has a detrimental impact on the trailing edge source. This last observation is explained by the fact that the impact of turbulence on the leading edge of the blade induces pressure fluctuations, but it also increases the robustness of the boundary layer (which are laminar on a large part of the chord due to the low Reynolds number).

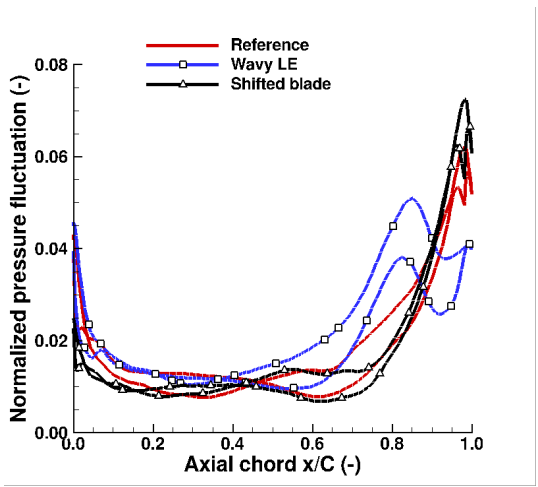


Figure 15: Influence of the geometry on the mean normalized pressure fluctuations $p' / (\frac{1}{2}\rho(\Omega.R)^2)$ along the rotor chord at $r/R = 0.75$.

A Power-Spectrum Density (PSD) of pressure signals is performed at 10 radii from the rotor. At this location, only acoustic fluctuations remain, so such a PSD gives an estimation of the far-field noise generated by the propeller. For the reference geometry, the dominant frequency is $f = 3/\Omega = 3f_{rotor}$, which corresponds to the blade passing frequency. The first ($f = 6f_{rotor}$) and the second harmonic ($f = 9f_{rotor}$) are also well highlighted. For the wavy leading edge geometry, the dominant frequency is still the blade passing frequency, but the amplitude of the first and second harmonics have been reduced compared to the reference geometry. For the shifted blade geometry, the dominant frequency is now the rotor frequency (the flow field is no longer uniform on the three blades), and the amplitude of the blade passing frequency is reduced. The frequency $f = 5f_{rotor}$ also emerges in the flow, induced by the interaction between the rotor blades.

The global noise of each configuration can be evaluated by integrating the pressure signal for all frequencies, which gives a total noise of 1) 64.9dB (reference geometry), 2) 64.1 dB (wavy leading edge) and 3) 68.4 dB (shifted blade). Only the wavy leading edge successfully reduces the total far-field noise.

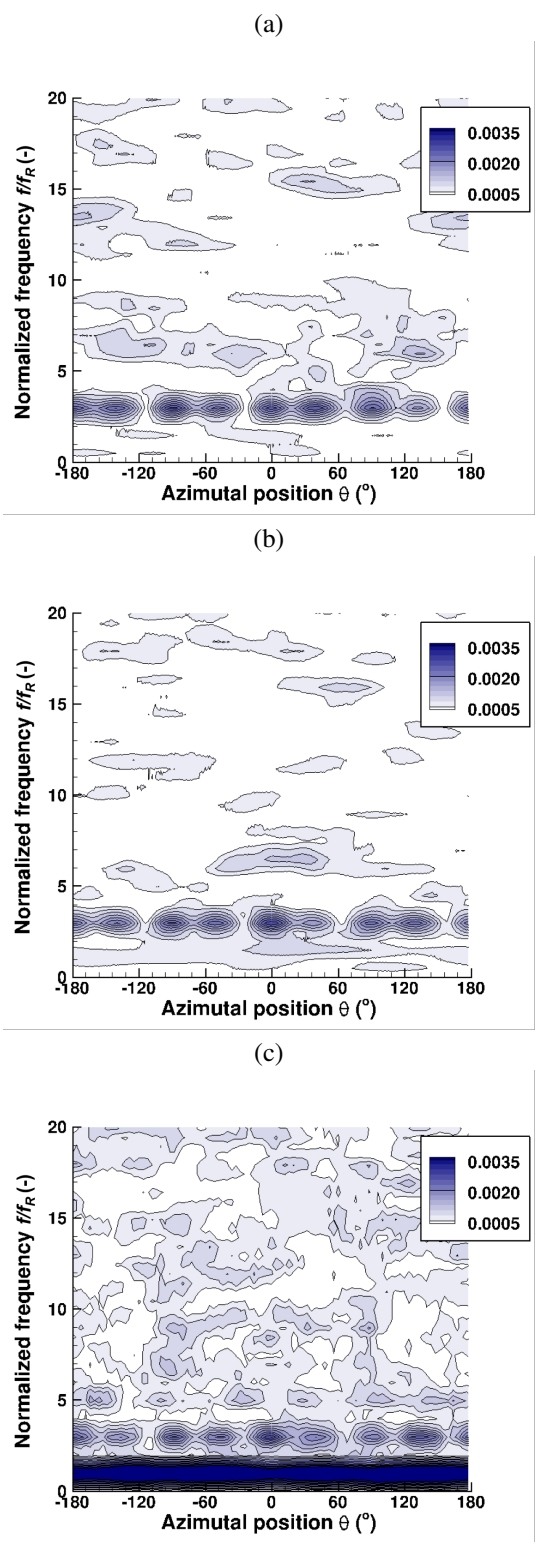


Figure 16: Power Spectrum Density of pressure signals at 10 radii from the rotor. Frequency is normalized with the rotor frequency ($f_R = 82.5$ Hz).

While the reduction of only 0.8 dB is rather modest, this reduction should be combined with the increase in rotor thrust coefficient that allows to decrease the rotor speed for a given thrust. For example, following Powell [30], the total noise for a jet scales as the velocity V^8 . If this relation could be verified for propeller, this could result in an additional 1dB reduction on the total noise.

CONCLUSION

A numerical campaign has been performed on three rotor geometries, suitable for micro-UAV. The objectives of this work were to analyze the turbulent flow generated by the tip vortex of a rotor in hover (as a potential source of noise) and to study potential solutions to reduce the noise generated by the rotor. This work has been conducted using unsteady RANS and LES-LBM flow solvers. The comparison with measurements shows that: 1) LES-LBM accurately predicts the thrust coefficient but over-predicts the torque coefficient, 2) URANS over-predicts both the thrust and torque coefficients. The reduction in thrust as predicted with LES-LBM compared to URANS is due to a separation of the boundary layer on the suction side, in the vicinity of the rotor tip.

The analysis of the flow underlines the sensitivity of the tip vortex breakdown phenomenon to the turbulence modelling. A conclusion of this work is that at such low Reynolds number, there is a risk of vortex breakdown, which in turns can generate turbulence that interacts with the following blade, including in hover conditions. Such phenomenon is responsible for an increase of the total noise but it also increases the robustness of the boundary layer by injecting turbulence in a boundary layer that is laminar on a large part of the rotor chord. This point should be investigated in more details, especially regarding the state of the boundary layer.

Regarding turbulence, this work proposed a way to estimate the value of the Taylor microscale (which represent about 2% of the rotor radius R) and Kolmogorov length scale (which represents about 0.05% of the rotor radius R). To evaluate the typical length scale that should be controlled at the leading edge, the use of the Taylor microscale (that represents the typical distance on which an information remains coherent, e.g. the distance between two legs of a vortex) is probably more appropriate than an integral length scale (that represents the maximum distance on which a flow pattern will have an influence, e.g. the rotor radius).

Among the three designs tested, the use of a wavy leading edge is a promising solution to reduce noise, by a direct mechanism (for a given rotation speed, noise is reduced by 1dB) and by an indirect mechanism (for a given thrust, the rotation speed can be reduced by 3%, leading to another 1dB of reduction). The other solution consists in a shift of the rotor blades (in the streamwise direction). While this kind of geometry helps to reduce the noise associated to the blade passing frequency, it is counter-balanced by an increase of the

noise associated to the rotor frequency, leading to an increase of the total noise by 3.5dB.

Actually, some of the findings of this work (vortex breakdown, boundary layer separation) should be supported by additional experimental campaigns (using PIV) and numerical simulation (e.g. RANS with transition models or hybrid RANS/LES approaches).

ACKNOWLEDGEMENTS

This research is supported by the Direction Générale de l'Armement (DGA) from the French Ministry of Defense, so this support is acknowledged. The authors also thank the technical team for their support, specially Rémy Chanton and Sylvain Belliot. Numerical simulations have been performed thanks to the computing center of the Federal University of Toulouse (under projects CALMIP p1425 and p17014) and resources provided by GENCI. These supports are greatly acknowledged. Special thanks to Orestis Malaspinas and Jonas Latt, from the University of Geneva and FlowKit, for their support on Palabos. The authors also thank the development team of Antares (<http://cerfacs.fr/antares>) at CERFACS, for providing the software used for post-processing.

REFERENCES

- [1] A. Christian and R. Cabell. Initial investigation into the psychoacoustic properties of small unmanned aerial system noise. In *23rd AIAA/CEAS Aeroacoustics conference*, number 2017-4051, 2017.
- [2] M. Roger and S. Moreau. Extensions and limitations of analytical airfoil broadband noise models. *International J. of Aeroacoustics*, 9(3):273–305, 2010.
- [3] Y. H. Yu. Rotor blade-vortex interaction noise. *Progress in Aerospace Sciences*, 36:97–115, 2000.
- [4] F. N. Coton, R. A. Mcd., T. Wang, and S. J. Newman. A wind-tunnel based study of helicopter tail rotor blade vortex interaction. *Aeronautical Journal*, 108(1083):237–244, 2004.
- [5] N. M. Chaderjian and J. U. Ahmad. Detached eddy simulation of the UH-60 rotor wake using adaptive mesh refinement. In *Proceedings of the American Helicopter Society 68th Annual Forum*, number Forth Worth, USA, 2012.
- [6] R. Ghias, R. Mittal, H. Dong, and T. Lund. Large-eddy simulation of the tip flow of a rotor in hover. In *Proceedings of the 34th Fluid Dynamics Conference and Exhibit*, number AIAA 2004-2432, Portland, USA, 2004.
- [7] H. Winarto. *BEMT algorithm for the prediction of the performance of arbitrary propellers*. The Sir Lawrence Wackett centre for aerospace design technology, Royal Melbourne Institute of Technology, 2004.

- [8] M. Drela and M. B. Giles. Viscous-inviscid analysis of transonic and low Reynolds number airfoils. *AIAA J.*, 25(10):1347–1355, 1987.
- [9] H. Johari, C. Henoch, D. Cosutodio, and A. Levshin. Effects of leading edge protuberances on airfoil performance. *AIAA J.*, 45(11):2634–2642, 2007.
- [10] V. Clair, C. Polacsek, T. Le Garrec, and G. Reboul. Experimental and numerical investigation of turbulence-airfoil reduction using wavy leading edges. *AIAA J.*, 51(11):2695–2713, 2013.
- [11] P. Chaitanya, P. Joseph, S. Narayanan, C. Vanderwel, J. Turner, J. W. Kim, and B. Ganapathisubramani. Performance and mechanism of sinusoidal leading edge serrations for the reduction of turbulence-aerofoil interaction noise. *J. Fluid Mechanics*, 818:435–464, 2017.
- [12] C. M. Rhie and W. L. Chow. Numerical study of the turbulent flow past an airfoil with trailing edge separation. *AIAA J.*, 21:1525–1532, 1983.
- [13] J. H. Ferziger and M. Peric. *Computational Methods for Fluid Dynamics*, volume 3rd rev. ed. Springer-Verlag, Berlin, 2002.
- [14] N. Gourdain, D. Singh, T. Jardin, and S. Prothin. Analysis of the turbulent wake generated by a micro-air vehicle hovering near the ground with a Lattice Boltzmann Method. *J. American Helicopter Society*, to be published.
- [15] P. Lallemand and L. S. Luo. Theory of the lattice Boltzmann method: dispersion, dissipation, isotropy, Galilean invariance, and stability. *Phys. Rev. E.*, 61(6):6546–6562, 2000.
- [16] D. D’Humières, I. Ginzburg, M. Krafczy, P. Lallemand, and L. S. Luo. Multiple relaxation time lattice Boltzmann models in three-dimensions. *Phil. Trans. R. Soc. A*, 360(1792):437–451, 2002.
- [17] I. Ginzburg, F. Verhaeghe, and D. D’Humières. Study of simple hydrodynamic solutions with the two-relaxation-times lattice Boltzmann scheme. *Commun. Comput. Phys.*, 3:519–581, 2008.
- [18] J. Latt and B. Chopard. Lattice Boltzmann method with regularized non-equilibrium distribution functions. *Math. Comp. Sim.*, 72:165–168, 2006.
- [19] O. Malaspinas, B. Chopard, and J. Latt. General regularized boundary condition for multi-speed lattice boltzmann models. *J. Computer and Fluids*, 49:29–35, 2011.
- [20] P. Sagaut. Toward advanced subgrid models for lattice Boltzmann based large-eddy simulation: theoretical formulations. *Computers and mathematics with applications*, 59(7):2194–2199, 2010.
- [21] D. J. Bodoni. Analysis of sponge zones for computational fluid mechanics. *J. Computational Physics*, 212(2):681–702, 2006.
- [22] T. Inamuro. Lattice boltzmann methods for moving boundary. *Fluid Dyn. Res.*, 44(2):024001, 2012.
- [23] O. Malaspinas and P. Sagaut. Wall model for large eddy simulation based on the lattice Boltzmann method. *J. Computational Physics*, 275:25–40, 2014.
- [24] W. K. George. Lectures in turbulence for the 21st century. Technical report, Imperial College of London, 2013.
- [25] O. Lucca-Negro and T. O’Doherty. Vortex breakdown: a review. *Progress in Energy and Combustion Science*, 27(431-481), 2001.
- [26] R. E. Spall, T. B. Gatski, and C. E. Grosh. A criterion for vortex breakdown. *Physics of Fluids*, 30(11):3434, 3440 1987.
- [27] S. Morton, J. Forsythe, A. Mitchell, and D. Hajek. DES and RANS simulations of delta wing vortical flows. In *40th AIAA Aerospace Sciences Meeting and Exhibit*, number AIAA 2002-0587, 2002.
- [28] S. B. Muller and L. Kleiser. Large Eddy Simulation of vortex breakdown in compressible swirling jet flow. *Computers & Fluids*, 37:844–856, 2008.
- [29] I. Mary. Large Eddy Simulation of vortex breakdown behind a delta wing. *Heat and fluid flow*, 24:596–605, 2003.
- [30] A. Powell. On the generation of noise by turbulent jets. In *ASME publications*, number paper 59-AV-53, 1958.